Collapse risk and residual drift performance of steel buildings using post-tensioned MRFs and viscous dampers in near-fault regions

A. S. Tzimas[1], G. S. Kamaris[1], T. L. Karavasilis[1,*] and C. Galasso[2]

[1] School of Engineering, University of Warwick, Coventry CV4 7AL, United Kingdom
[2] Department of Civil, Environmental & Geomatic Engineering & Institute for Risk and Disaster Reduction, University College London (UCL), London WC1E 6BT, United Kingdom

Abstract: The potential of post-tensioned self-centering moment-resisting frames (SC-MRFs) and viscous dampers to reduce the collapse risk and improve the residual drift performance of steel buildings in near-fault regions is evaluated. For this purpose, a prototype steel building is designed using different seismic-resistant frames, i.e.: moment-resisting frames (MRFs); MRFs with viscous dampers; SC-MRFs; and SC-MRFs with viscous dampers. The frames are modeled in OpenSees where material and geometrical nonlinearities are taken into account as well as stiffness and strength deterioration. A database of 91 near-fault, pulse-like ground motions with varying pulse periods is used to conduct incremental dynamic analysis (IDA), in which each ground motion is scaled until collapse occurs. The probability of collapse and the probability of exceeding different residual story drift threshold values are calculated as a function of the ground motion intensity and the period of the velocity pulse. The results of IDA are then combined with probabilistic seismic hazard analysis models that account for near-fault directivity to assess and compare the collapse risk and the residual drift performance of the different seismic-resistant frames. The paper highlights the benefit of combining the post-tensioning and supplemental viscous damping technologies in the near-source. In particular, the SC-MRF with viscous dampers is found to achieve significant reductions in collapse risk and probability of exceedance of residual story drift threshold values compared to the MRF.

Keywords: Self-centering; Post-tensioned; Steel frames; Dampers; Collapse; Residual drifts; Near-fault; Seismic hazard analysis; Seismic Risk

*Corresponding Author: Theodore L. Karavasilis, Associate Professor of Structural Engineering
School of Engineering, University of Warwick, Coventry CV4 7AL, United Kingdom
E-mail address: T.Karavasilis@warwick.ac.uk

1 Introduction

A distinct velocity pulse with a long period often characterizes near-fault earthquake ground motions. Such pulse is typically observed at the beginning of the fault-normal (FN) ground velocity time-history and has a probability of occurrence that depends on the site-to-source geometry, earthquake magnitude and other parameters (Somerville et al. 1997; Iervolino and Cornell 2008). Starting from the pioneer studies of Veletsos and Newmark (1960) and Bertero et al. (1978), the response of yielding single-degree-of-freedom systems subjected to near-fault earthquake ground motions has been extensively studied (Chopra and Chintanapakdee 2003; Mavroeidis et al. 2004 and references therein). Other studies focused on yielding frames and showed the potential of near-fault ground motions to induce large story drifts (Alavi and Krawinkler 2004; Makris and Psychogios 2006; Karavasilis et al. 2010 and references therein).

The destructive potential of near-fault ground motions was evident after many earthquakes such as the Northridge, California (1994); Kobe, Japan (1995); Chi-Chi, Taiwan (1999); and L'Aquila, Italy (2009). These earthquakes highlighted the limitations of conventional seismic-resistant systems, which experience significant inelastic deformations in main structural members and appreciable residual story drifts. The latter are recognized as an important seismic performance index that is directly related to the probability of demolition of a building. For example, McCormick et al. (2008) concluded that, in Japan, it was generally less costly to demolish and rebuild a steel building than to repair it when residual story drifts were higher than 0.5%. It is emphasized that residual displacements show significant record-to-record variability compared to peak displacements (Ruiz-Garcia and Miranda 2006), and therefore, significant uncertainty is involved when designing conventional yielding structures to be reparable in the aftermath of strong earthquakes. Moreover, current seismic design codes do not account for the potential of near-fault ground motions to induce large residual story drifts.

Modern seismic codes in the USA have adopted risk-targeted seismic design maps, which define design spectral acceleration values that are intended to ensure that newly designed buildings have a uniform probability of collapse of 1% in 50 years (Luco et al. 2007). However, in their current form, they do not explicitly account for the potentially higher collapse risk of buildings located in near-fault regions. A recent study highlighted the need to account for such higher collapse risk by showing that the probability of collapse in 50 years of reinforced concrete buildings at a representative near-fault site is approximately 6%, i.e. significantly higher than the aforementioned 1% limit (Champion and Liel 2012).

The issues of large residual story drifts and higher collapse risk in near-fault regions could be addressed by employing modern resilient structures instead of the conventional yielding ones, which are promoted by current seismic design codes such as the Eurocode 8 (EC8 2013). Steel self-centering moment-resisting frames (SC-MRFs) using post-tensioned (PT) beam-column connections are a promising class of resilient structures that exhibit softening force-drift behavior and eliminate beam inelastic deformations and residual drifts (Ricles et al. 2001; Christopoulos et al. 2002; Rojas et al. 2004; Kim and Christopoulos 2008a; Tsai et al. 2008; Chou and Lai 2009; Chou et al. 2009; Wolski et al. 2009; Vasdravellis et al. 2013a,b; Dimopoulos et al. 2013). Seismic design procedures for SC-MRFs are proposed in (Garlock et al. 2007; Kim and Christopoulos 2008b). Steel moment-resisting frames (MRFs) equipped with passive dampers are another class of resilient structures, which can be generally designed to be lighter and perform better than steel MRFs (Karavasilis et al. 2011, 2012). However, a study shows that supplemental viscous damping does not always ensure adequate reduction of residual drifts (Karavasilis and Seo 2011). Moreover, a recent work shows that supplemental viscous damping does not guarantee higher

collapse resistance when the strength of the steel MRF with dampers is lower or equal to 75% of the strength of a steel MRF (Seo et al. 2014). Few studies investigated the effectiveness of combining self-centering systems with viscous dampers to increase seismic resilience. The use of viscous dampers in parallel to self-centering rocking walls has been proposed as an effective way to control peak story drifts and residual drifts (Kurama 2000). The parallel combination of hysteretic and viscous energy dissipation along with a friction slip mechanism in series connected to the viscous energy dissipation mechanism were found to achieve high levels of seismic performance (Kam et al. 2010). The parallel use of viscous dampers and steel SC-MRFs was found capable to simultaneously control inelastic deformations, peak storey drifts, and residual storey drifts (Tzimas et al. 2015).

The potential of using in parallel SC-MRFs and viscous dampers with the goal of reducing the collapse risk and the probability of demolition (due to large residual story drifts) of steel buildings in near-fault regions has never been assessed. In this paper, a prototype steel building is designed using different seismic-resistant frames, i.e.: MRFs; MRFs with viscous dampers; SC-MRFs; and SC-MRFs with viscous dampers. The frames are modeled in OpenSees (Mazzoni et al. 2006) where material and geometrical nonlinearities are taken into account as well as stiffness and strength deterioration. A database of 91 near-fault, pulse-like ground motions with varying pulse periods is used to conduct incremental dynamic analysis (IDA) (Vamvatsikos and Cornell 2002), in which each ground motion is increasingly scaled until collapse occurs. The probability of collapse and the probability of exceeding different residual story drift threshold values are then calculated as a function of the ground motion intensity and the period of the velocity pulse. Finally, the results of IDA are combined with probabilistic seismic hazard analysis models that account for near-fault directivity to assess and compare the collapse risk and the residual drift performance of the different seismic-resistant frames.

2. PT connection with WHPs

Fig. 1a shows a SC-MRF using PT connections with web hourglass shape pins (WHPs) and Fig. 1b shows an exterior PT connection with WHPs. This PT connection has been experimentally and numerically evaluated by Vasdravellis et al. (2013a,b). Two high strength steel bars located at the mid depth of the beam, one at each side of the beam web, pass through holes drilled on the column flanges. The bars are post-tensioned and anchored to the exterior columns. WHPs are inserted in aligned holes on the beam web and on supporting plates welded to the column flanges. Energy is dissipated through inelastic bending of the WHPs that have an optimized hourglass shape (Fig. 1c) with enhanced fracture capacity. The beam web and flanges are reinforced with steel plates. The panel zone is strengthened with doubler and continuity plates. A fin plate welded on the column flange and bolted on the beam web is used for easy erection and resistance against gravity loads before post-tensioning. Slotted holes on the beam web ensure negligible influence of the fin plate on the PT connection hysteretic behavior.

The connection behavior is characterized by gap opening and closing in the beam-column interface and re-centering capability as the result of the force in the PT bars. Fig. 2a shows the free body diagram of an external PT connection where d_{1u} and d_{1l} are the distances of the upper and lower WHPs from the center of rotation that is assumed to be at the inner edge of the beam flange reinforcing plates; d_2 is the distance of the PT bars from the center of rotation; T is the total force in both PT bars; $F_{WHP,u}$ and $F_{WHP,l}$ are the forces in the upper and lower WHPs; C_F is the compressive force in the beam-column interface; V_{C1u} and V_{C1l} are the shear forces in the upper and lower column, M is the PT connection moment, V is the beam shear force; and N is the horizontal clamping force that is transferred to the beam-column

interface through the slab diaphragm and the beam. Fig. 2b shows the SC-MRF expansion due to rotations θ in the PT connections. Fig. 2c shows the theoretical cyclic moment-rotation (M-θ) behavior of the PT connection. After decompression of the PT connection (Point 1 in Fig. 2c), gap opens and the behavior becomes nonlinear elastic with rotational stiffness S_1. At point 2, the upper WHPs yield and M continues to increase with slope S_2. At point 3, the lower WHPs yield and M continues to increase with slope S_3. When loading is reversed, the connection begins to unload until the gap closes. Equations to calculate S_1 to S_3 and θ_1 to θ_3 are provided in (Tzimas et al. 2015).

(a)

(b)   (c)
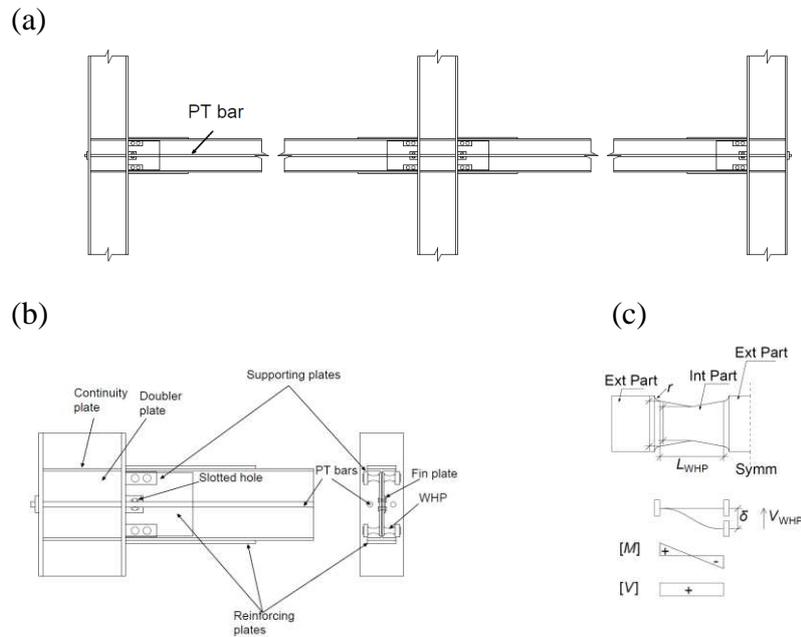

Fig. 1 a) SC-MRF; **b)** exterior PT connection with WHPs; and **c)** half WHP geometry and assumed static system.

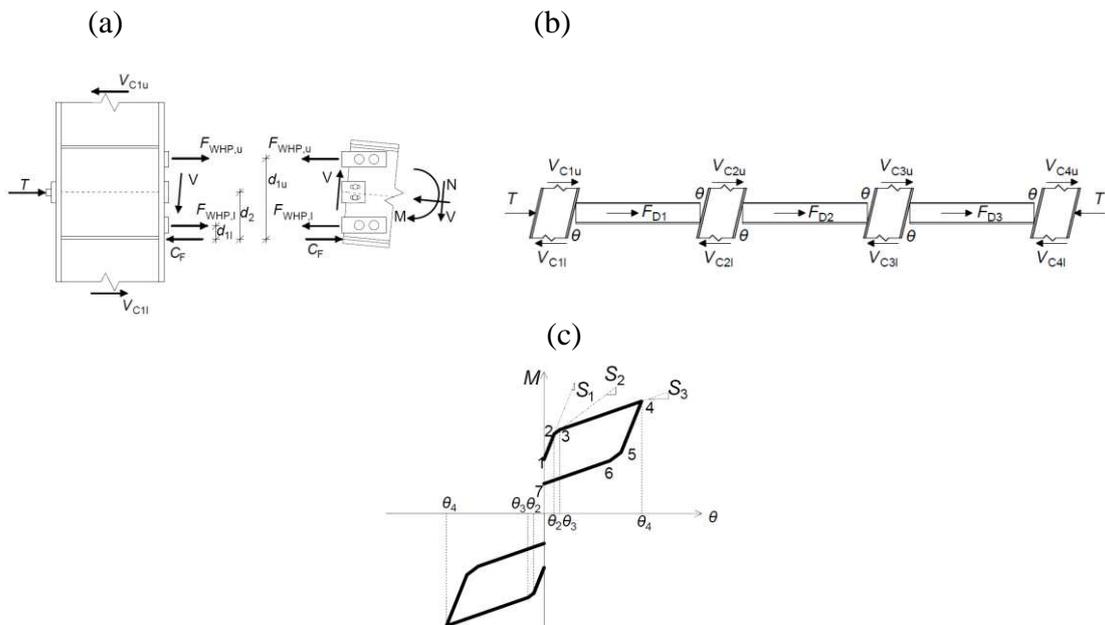(a)   (b)

(c)

Fig. 2 a) Free body diagram of an external PT connection with WHPs; **b)** SC-MRF expansion and horizontal forces equilibrium; and **c)** theoretical cyclic behavior of the PT connection

3. Prototype building and design of the seismic-resistant frames

Fig. 3a shows the plan view of a 5-storey, 5-bay by 3-bay prototype steel building having two identical perimeter seismic-resistant frames in the 'x' plan direction. The study focuses on one perimeter seismic-resistant frame, which is designed as a high ductility class MRF, MRF with viscous dampers, SC-MRF, and SC-MRF with viscous dampers using existing design procedures (Garlock et al. 2007; Kim and Christopoulos 2008b; Tzimas et al. 2015). These different designs of the perimeter seismic-resistant frame have the same beam and column cross-sections. Viscous dampers are installed in the interior gravity frames (with pinned beam-column and pinned column base connections) that are coupled with the perimeter seismic-resistant frame through the floor diaphragm as shown in Fig. 3b. The building has ductile non-structural elements, and so, the maximum interstory drift ratio, $\theta_{s,max}$, should be lower than 0.75% under the frequently occurred earthquake (FOE) according to EC8 (2013). The design basis earthquake (DBE) is expressed by the Type 1 elastic response spectrum of EC8 (2013) with peak ground acceleration equal to 0.35g and ground type B. The FOE has intensity of 40% (reduction factor v=0.4 in EC8 (2013)) the intensity of the DBE. The maximum considered earthquake (MCE) has intensity of 150% the intensity of the DBE. The model used for design is based on the centerline dimensions of the seismic-resistant frame without accounting for the finite panel zone dimensions. The steel yield strength is equal to 355 MPa for the columns, 275 MPa for beams, 930 MPa for PT bars, 235 MPa for the WHPs and 275 MPa for the beam reinforcing plates. Nonlinear viscous dampers are designed with a horizontal configuration (as shown in Fig. 3b) and a velocity exponent equal to 0.5 to achieve a total damping ratio equal to 20% at the first fundamental period, which is equal to $T_1=1.27$ s. The inherent damping of all frames is 3%. The estimated $\theta_{s,max}$ under the DBE is equal to 1.2% and 1.8% for the frames with and without viscous dampers, respectively. The total damping ratio was determined for damper deformation amplitudes corresponding to $\theta_{s,max}$ under the DBE, and, a lateral story stiffness proportional distribution of the damping constants. The SC-MRF and the MRF with viscous dampers have the same total damping ratio. Design data of the frames are given in Table 1.

(a) (b)
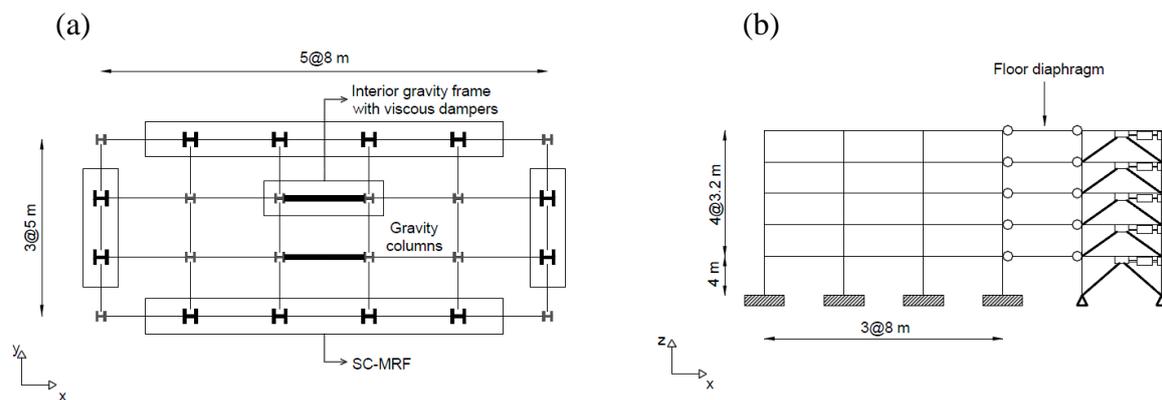
Fig. 3 a) Plan; and **b)** elevation of the prototype building.

Table 1 Design data for the MRF, SC-MRF, MRF with viscous dampers, and SC-MRF with viscous dampers

Story	Cross-sections		PT force	PT bar diameter	PT connections design data					Viscous dampers
					WHP ext. diameter	WHP int. diameter	WHP length	Reinf. plate length	Reinf. plate thickness	
	Beam	Column	kN	mm	mm	mm	mm	mm	mm	kN·(s./m)^0.5
1	IPE550	HEB650	1087	50	43	33	70	1392	35	2139
2	IPE600	HEB650	1256	60	46	36	70	1660	46	1641
3	IPE550	HEB650	1087	48	43	33	70	1416	35	1416

4	IPE500	HEB600	941	38	41	30	70	1092	26	1102
5	IPE500	HEB600	941	36	39	28	70	743	22	810

4. Nonlinear models

Models for the SC-MRF are developed in OpenSees (Mazzoni et al. 2006) as shown in Fig. 4. The columns and the reinforced lengths of the beams are modeled as nonlinear force-based beam-column fiber elements with bilinear elastoplastic stress-strain behavior. The assumption of stable hysteresis for the columns is justified because heavy columns with webs and flanges of low slenderness do not show cyclic deterioration even under large drifts (Newell and Uang 2006). The unreinforced lengths of the beams are modeled using force-based beam-column fiber elements with end hinges (Scott and Fenves 2006). The modified Ibarra-Krawinkler model (Lignos and Krawinkler 2011) is used for the stress-strain cyclic behavior of the fibers to capture stiffness and strength deterioration due to beam local buckling just after the end of the beam flange reinforcing plates. This modeling approach results in smooth hysteretic curves for flexural members similar to that observed in experiments (Hamidia et al. 2014) and also captures the axial force (due to initial post-tensioning) – bending moment interaction in the beams of the SC-MRF. Panel zones are modeled using the model in (Krawinkler 1978). To account for P-Δ effects, the gravity columns associated with the SC-MRFs are modeled as lean-on columns. Diaphragm action is modeled with truss elements connecting the lean on columns nodes to nodes defined along the length of the beams at the points where secondary beams are placed. These trusses have stiffness of 100 times the axial beam stiffness. The dampers are modeled with zero length viscous elements, while the damper supporting braces are modeled with elastic braces, as they are strong enough to avoid buckling. In the analytical model, the damper limit states caused by their stroke limit are not considered, i.e. it is assumed that dampers will be manufactured with enough stroke to avoid reaching their limit states even under very large story drifts.
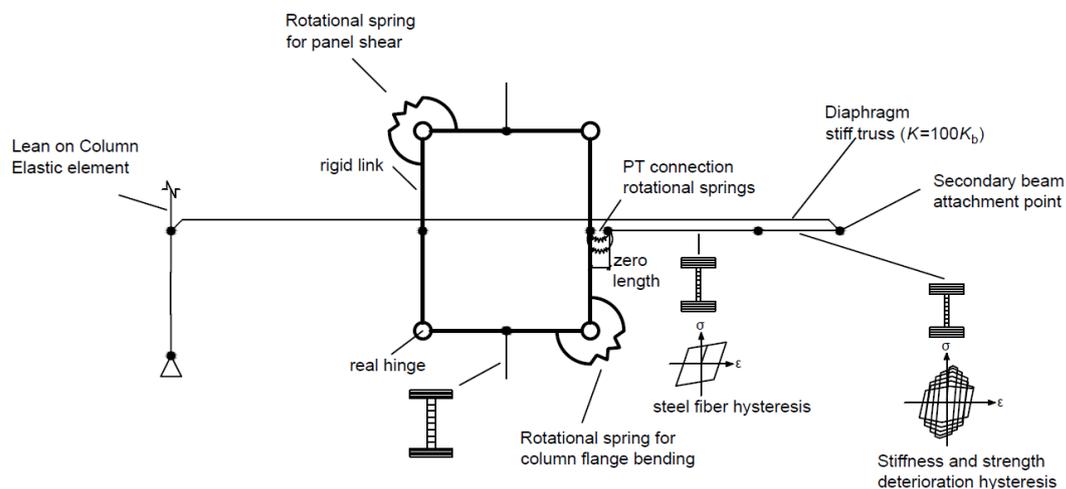
Fig. 4 Simplified nonlinear model for an exterior PT connection and the associated beams and columns.

The cyclic M-θ behavior of the PT connections is simulated by using 2 parallel rotational springs at the beam ends. The first spring is nonlinear elastic and simulates the contribution of the PT bars on the rotational behavior of the PT connection, while the second spring is bilinear elasto-plastic and simulates the contribution of the WHPs. The properties of these

springs can be determined using equations available in Tzimas et al. (2015). The accuracy of this simplified model is evaluated against the detailed model in Tzimas et al. (2015), which is based on contact and hysteretic springs at the beam-column interface. Fig. 5a compares the base shear coefficient (V/W; V: base shear and W: seismic weight)-roof drift (θ_r) behaviors from nonlinear monotonic static (pushover) analysis, while Fig. 5b compares the V/W-θ_r behaviors from nonlinear cyclic static (push-pull) analysis of the SC-MRF using either the simplified or the detailed PT connection model.

The connections of the MRF are assumed to be rigid and have full strength, while beams are modeled as elastic elements with zero length rotational springs at their ends that exhibit strength and stiffness deterioration (Lignos and Krawinkler 2011). The columns and panel zones of the MRF are modeled as described above for the SC-MRF.

The OpenSees models for the SC-MRF and the conventional MRF include the effect of the panel zone stiffness, and so, result in T_1 values shorter than 1.27 s, which is based on the centerline models used for design. T_1 from the OpenSees models is 0.94 s for the SC-MRF and 1.18 s for the MRF.
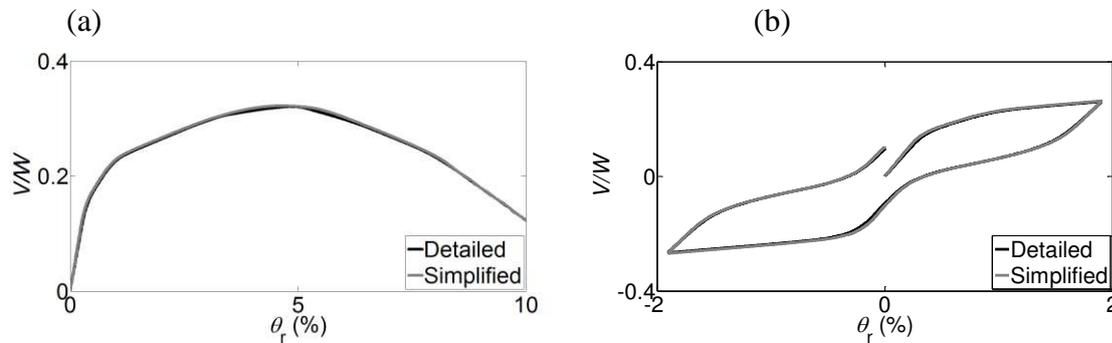

Fig. 5 Comparison of the **a)** monotonic static (pushover); and the **b)** cyclic static (push-pull) behaviors of the SC-MRF using either the simplified or the detailed model in Tzimas et al. (2015) for the PT connections.

5 Ground motions considered

A set of 91 pulse-like ground motions is used for nonlinear dynamic time history analyses. These ground motions were selected by Baker (2007) from the PEER NGA (2015) using wavelet analysis to detect and determine the pulse period, T_p. Only FN ground motions having a minimum peak ground velocity of 30cm/s are included in this set. Ground motions were recorded from earthquakes with moment magnitudes, M, varying from 5.0 to 7.6 and include pulse periods that vary between 0.4 and 12.9 s. Although all of the records exhibit velocity pulses, site-to-source distances were not considered in the selection criteria and range from 0.10 to 102 km. Thus, some of the observed pulses were probably caused by other geological mechanisms, such as basins. A complete list of the pulse-like ground motions used in this study can be found in Baker (2007).

In this study, the collapse risk of the building depends on the probability of occurrence or not of a pulse-like ground motion and is calculated through the theorem of total probability. For this reason, a second set of far-field records is needed for the determination of the probability of collapse for sites that are not influenced by forward directivity effects. Similarly to Champion and Liel (2012), the set of far-field ground motions used in this study is based on the FEMA P695 (2008) far-field ground motion set, which includes 22 record pairs, each with two horizontal components for a total of 44 ground motions. Those ground motions are recorded at sites located greater than or equal to 10 km from fault rupture. Event

magnitudes range from M 6.5 to M 7.6 with an average magnitude of M 7.0. It is worth noting that the ground motion records were selected without consideration of spectral shape. In fact, the FEMA P695 (2008) far-field ground motion set consists of records that are structure type and site hazard independent.

6 Collapse evaluation

The collapse risk of each frame is assessed using IDA (Vamvatsikos and Cornell 2002), i.e. the frame model is subjected to a specific ground motion that is increasingly scaled until collapse occurs. The spectral acceleration at T_1 of the frame, $S_a(T_1)$, is used as the seismic intensity measure (IM) and $\theta_{s,max}$ is the response parameter to be monitored. Fig. 6a shows the IDA curves for the SC-MRF with viscous dampers and the set of the far-field ground motions. For each design case and ground motion, the collapse $S_a(T_1)$ value at which $\theta_{s,max}$ increases without bound was obtained. A Rayleigh damping matrix was used to model the inherent 3% critical damping at the first two modes of vibration. Each dynamic analysis was extended well beyond the actual earthquake time to allow for damped free vibration decay and accurate residual story drifts, $\theta_{s,res}$, calculation.

A collapse fragility curve is constructed by fitting a lognormal cumulative distribution function to the collapse $S_a(T_1)$ values of each frame. The median value and the lognormal standard deviation of the ground motion intensities at which collapse occurs in IDA define this distribution. The collapse fragility curve of the SC-MRF with viscous dampers is shown in Fig. 6b with a solid line together with the results from the numerical analyses.
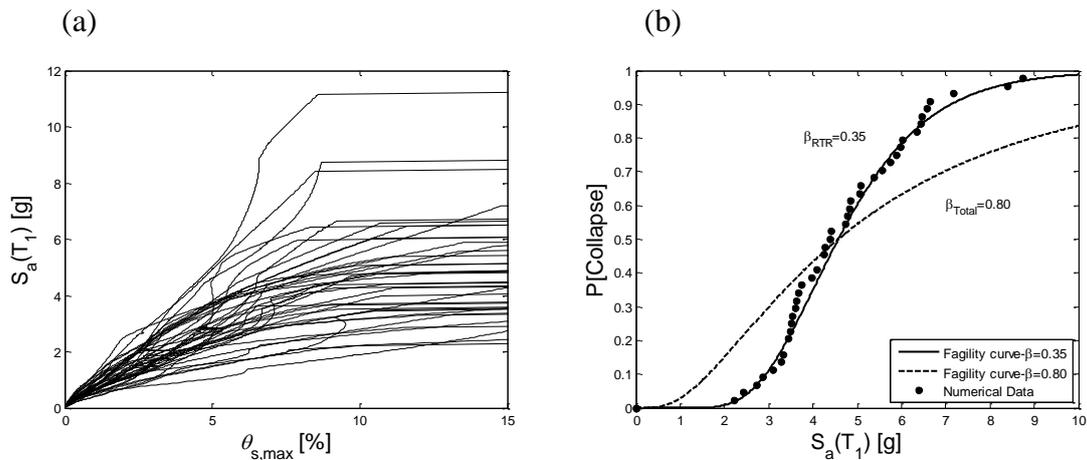

Fig. 6 a) IDA curves of the SC-MRF with viscous dampers; and **b)** corresponding collapse fragility curve.

The lognormal standard deviation, β, influences the shape of the fragility curve and reflects the level of uncertainty in the analysis results. Two sources of uncertainty in quantifying the collapse $S_a(T_1)$ value of structural systems can be considered, i.e. aleatory and epistemic. The aleatory or record-to-record uncertainty (β_{RTR}) reflects the variability in the response of the structures due to the random nature of ground motions. The epistemic or modeling uncertainty ($\beta_{modeling}$) is mainly due to lack of knowledge about the real properties of the structural elements. To combine the record-to-record and modeling uncertainties, the mean estimates approach (Liel et al. 2009) assumes that the two uncertainties are lognormally distributed and independent, such that the total uncertainty, β_{Total}, is given by:

$$\beta_{\text{Total}} = \sqrt{\beta_{\text{RTR}}^2 + \beta_{\text{modeling}}^2} \qquad (1)$$

Similarly to Champion and Liel (2012), the value of β_{Total} is taken as 0.80, which may lead to slightly conservative absolute values of collapse risk. For example, the risk-targeted hazard maps in the USA use 0.6, which is consistent with typical values found in modeling uncertainty studies (e.g. Liel et al. 2009). However, different values of β_{Total} would change the absolute value of collapse risk assessments, but would not affect the relative comparison among the frames. The fragility curves shown in Fig. 6b have not been adjusted to account for the distinct spectral shape of rare ground motions, which can be characterized by the parameter ε proposed by Baker and Cornell (2006). The fragility curves presented in the following sections of the paper have been adjusted to consider the effect of ε using the methodology proposed by Haselton et al. (2011).

The risk assessment procedure for the near fault ground motions is properly modified to take into account the effect of the pulse period of the record, T_p, and is based on the approach proposed by Champion and Liel (2012), which is described in the following sections.

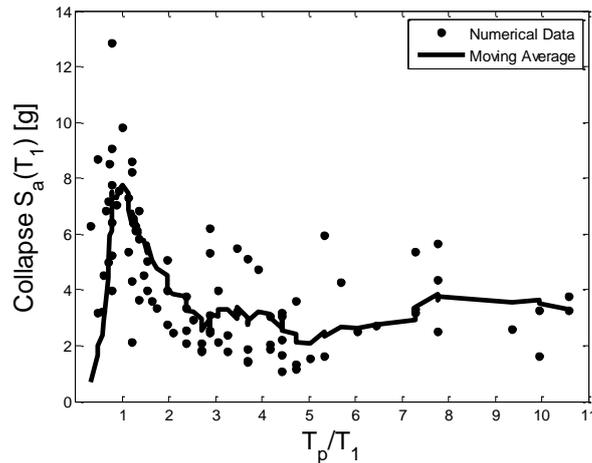## 7 Effect of pulse period in collapse assessment

Fig. 7 Collapse $S_a(T_1)$ of the SC-MRF with viscous dampers versus the T_p/T_1 ratio together with the generated moving average curve.
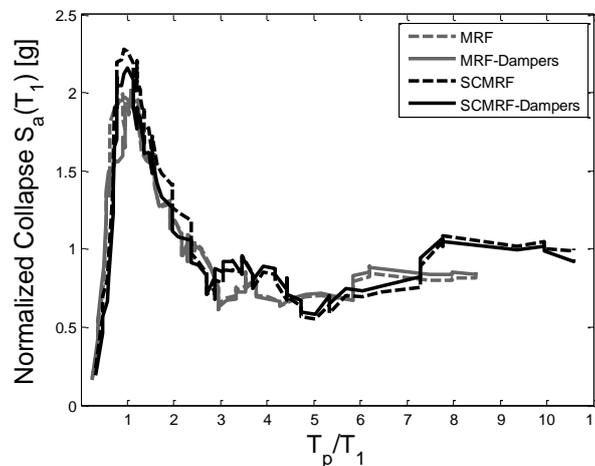

Fig. 8 Moving average curves representing normalized collapse $S_a(T_1)$ as a function of T_p/T_1 for all the frames.

Fig. 7 plots the collapse $S_a(T_1)$ values of the SC-MRF with viscous dampers versus the ratio T_p/T_1. In addition, the moving average of the numerical data is computed by averaging the point of interest with the five previous and subsequent data points. This is done to fit the data points with a trend-line in order to investigate the behavior of collapse $S_a(T_1)$. The maximum values of collapse $S_a(T_1)$ are obtained in the region of the moving average curve where the fundamental period, T_1, of the frame is approximately equal to T_p, i.e. $T_p/T_1 \approx 1$. This result is not consistent with the response of elastic structures, which experience their peak displacement demand for $T_p/T_1 \approx 1$, but is justified by the significant effective period elongation of the frame due to the large inelastic deformations associated with the collapse limit state. Fig. 7 shows that ground motions with a longer pulse period result in lower collapse $S_a(T_1)$. In addition, the collapse $S_a(T_1)$ of the frame tends to decrease in the region where $T_p < T_1$. Fig. 8 shows the moving average curves for all the frames, which are normalized by the median collapse $S_a(T_1)$ of each frame for all the near-field records. It is illustrated that all frames follow the same trend with slight variations.

8 Collapse fragility functions including near-fault directivity

As shown in the previous section, the collapse resistance of the frames depends not only on $S_a(T_1)$, but also on whether a ground motion exhibits a velocity pulse or not. To incorporate this effect in the collapse fragility functions, the theorem of total probability is utilized to calculate the probability of collapse, $P[Col|S_a = x]$, given a specific value of $S_a(T_1)$, i.e. the fragility function is given by (Champion and Liel 2012):

$$P[Col\,|\,S_a = x] = P[Col\,|\,S_a = x, Pulse] \cdot P[Pulse\,|\,S_a = x] + P[Col\,|\,S_a = x, NoPulse] \cdot P[NoPulse\,|\,S_a = x] \quad (2)$$

where $P[Col|S_a = x, Pulse]$, $P[Col|S_a = x, No\ Pulse]$, $P[Pulse|S_a = x]$ and $P[No\ Pulse|S_a = x]$ are the probability of collapse for pulse like ground motions, the probability of collapse for far-fault ground motions, the probability that a ground motion record exhibits a velocity pulse and the probability that a ground motion record does not exhibit a velocity pulse, respectively.

The term $P[Col|S_a = x, No\ Pulse]$ is determined from the fragility curves constructed for the far-fault ground motions. The collapse probability when a pulse occurs, $P[Col|S_a = x, Pulse]$, depends on the pulse period and the likelihood of different pulse periods occurring, $P[T_p = t_i|S_a = x, Pulse]$:

$$P[Col\,|\,S_a = x, Pulse] = \sum_{i=1}^{All\ T_p} P[Col\,|\,T_p = t_i, S_a = x, Pulse] \cdot P[T_p = t_i\,|\,S_a = x, Pulse] \quad (3)$$

The probability of collapse for a given T_p value, $P[Col|T_p = t_i, S_a = x, Pulse]$, is computed through the moving average curve. The moving average represents the median collapse $S_a(T_1)$ as a function of T_p. For any value of T_p and $S_a(T_1)$, the probability of collapse is computed by assuming a lognormal distribution with a median equal to the value of $S_a(T_1)$ of the moving average for the given T_p and a standard deviation $\beta_{Total} = 0.8$.

The remaining parts of Equations (2) and (3) are computed with the aid of probabilistic seismic hazard analysis (PSHA), which provides the mean annual frequency, λ, of exceeding a seismic intensity measure (IM) level, x. Conventional far-field PSHA gives λ according to the following equation:

$$\lambda_{IM>x} = \sum_{i=1}^{N} \nu_i \int_m \int_r P[IM > x \mid m, r] f_{M,R}(m, r) dm dr \qquad (4)$$

where ν_i is the mean annual rate of earthquakes occurrence on a nearby fault i, N is the total number of faults, M is the moment magnitude, R is the source-to-site distance and $f_{M,R}$ is the joint probability density function of M and R. The expression $P[IM > x \mid m, r]$ is the probability that the ground motion intensity exceeds a specific value, x, given an earthquake of magnitude m at distance r, which can be obtained from ground motion prediction equations (GMPEs).

PSHA has been recently modified to account for near source conditions, i.e., Near-source Probabilistic Seismic Hazard Analysis (NS-PSHA); more details, including implementation and applications, can be found in (Iervolino and Cornell 2008; Tothong et al. 2007; Shahi and Baker 2011; Chioccarelli and Iervolino 2010, 2013, 2014). According to this methodology, Equation (4) is adjusted to account for potential near-source directivity through an additional term, Z, which defines the site-to-source geometry:

$$\lambda_{IM>x} = \sum_{i=1}^{N} \nu_i \int_m \int_r \int_z P[IM > x \mid m, r, z] f_{M,R,Z}(m, r, z) dm dr dz \qquad (5)$$

In this case, the probability that a specific IM value is exceeded, $P[IM > x \mid m, r, z]$, depends on the probability of occurrence of a pulse, the distribution of possible pulse periods and the peculiar spectral shape induced by the pulse. The probability of a pulse occurring is a function of site-to-source geometry and decreases with distance from the fault and for shorter fault rupture lengths (Iervolino and Cornell 2008; Shahi and Baker 2011). The pulse period distribution is a function of earthquake magnitude, with larger magnitude events usually causing longer pulse periods (Shahi and Baker 2011; Somerville 2003).

When the NS-PSHA is conducted for a given IM level, the probability that a pulse occurs, $P[Pulse \mid S_a = x]$, can be calculated by the following equation:

$$P[Pulse \mid S_a = x] = \frac{\lambda_{S_a=x,Pulse}}{\lambda_{S_a=x,Total}} \qquad (6)$$

where $\lambda_{S_a=x,Pulse}$ is the mean annual frequency of $S_a = x$ when only pulse-like ground motions are considered and $\lambda_{S_a=x,Total}$ is the mean annual frequency of $S_a = x$ when both pulse-like and far-fault ground motions occur. Note that NS-PSHA is computed here as $\lambda_{S_a=x}$ rather than $\lambda_{S_a>x}$ to allow for combination with the collapse fragility curves. The hazard disaggregation of Eq. (6) is required for each spectral acceleration level of interest (from the collapse fragility); a similar disaggregation process can also be used to identify the contribution of each pulse period, t_i, to each spectral value, i.e. $P[T_p = t_1 \mid S_a = x, Pulse]$. Finally, the term $P[No Pulse \mid S_a = x]$ is derived through the following equation:

$$P[NoPulse \mid S_a = x] = 1 - P[Pulse \mid S_a = x] \qquad (7)$$

A fixed (characteristic) M 7 strike-slip (SS) fault is considered to compare the seismic performance of the frames. The single fault is 42 km long based on the median Wells and Coppersmith (1994) magnitude-scaling relation and is assumed to have a recurrence rate of

0.05 earthquakes per year. The location of earthquake epicenters is uniformly distributed along the fault, while six sites with site-to-source distances equal to 5, 10 and 15 km at the end ("End-of-Fault" sites) and midpoint ("Midfault" sites) of the fault line are considered as shown in Fig. 9a.

The probability of a pulse occurring is computed by using the model of Iervolino and Cornell (2008) and depends, in the case of a SS rupture, on the rupture-to-site distance, R, the distance from the epicenter to the site measured along the rupture direction, s, and the angle between the fault strike and the path from the epicenter to the site, θ. A similar model is has been also introduced by Shahi and Baker (2011). As noted in Chioccarelli and Iervolino (2014), a deterministic relationship between these parameters and rupture length, position of the rupture on the fault and epicenter location exists, allowing to easily simulate the uncertainty involved for the hazard computations. However, while rupture length and rupture position are, in principle, random variables, the application here is implemented in the simplifying hypothesis of fixed rupture and position, similarly to the applications in Chioccarelli and Iervolino (2014). Such a hypothesis appears to be acceptable if a single magnitude can be generated by the considered fault, as assumed in this study where the main focus is to compare the seismic performance of different structural systems rather than to investigate NS-PSHA.
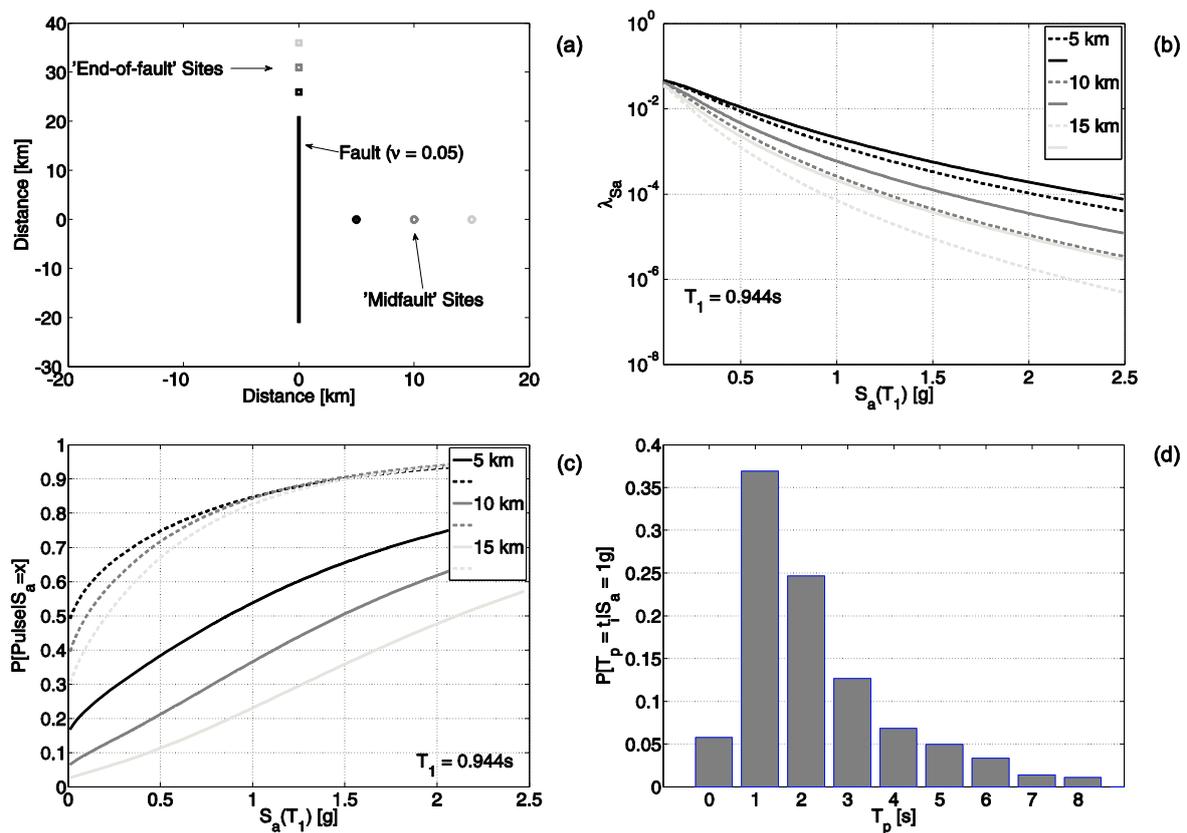
Fig. 9 Representative near-field sites considered in this study, showing **a)** site location and **b)** seismic hazard curves for the midfault (dashed lines) and end-of-fault (solid lines) sites with varying site-to-source distances. Hazard disaggregation results show **c)** the probability of pulse occurrence for the different sites at $S_a(T_1 = 0.944$ s) and **d)** a typical pulse period distribution for one hazard level, $S_a(T_1) = 1$ g, at the 5 km midfault site.

The pulse period prediction is based on the empirical model in Chioccarelli and Iervolino (2010). More details for the NS-PSHA calculations adopted herein, including the GMPE

modification to account for the 'bump' of spectral ordinates around the pulse period, can be found in Chioccarelli and Iervolino (2013).

NS-PSHA results are shown in Fig. 9b for $T_1 = 0.944$ s. Figs. 9c and d provide disaggregated hazard results in terms of $P[\text{Pulse}|S_a = x]$ and $P[T_p = t_i|S_a = x, \text{Pulse}]$ respectively (the latter refer to $S_a = 1$ g).

9. Seismic collapse risk assessment in the near-source

Using the methodology of the previous section, the collapse fragility curves of the frames for the case study of midfault sites at 15 km, are constructed and shown in Fig. 10a. The fragility curves show that the least susceptible structures to collapse are the frames equipped with viscous dampers, with the SC-MRF with viscous dampers exhibiting the lowest probabilities of collapse. Fig. 10b shows the fragility curves obtained for the SC-MRF with viscous dampers located at the midfault sites for site-to-source distances equal to 5, 10 and 15 km. It is observed that the probability of collapse is reduced with the distance from the fault, because the likelihood that a pulse occurs, $P[\text{Pulse}|S_a = x]$, decreases with distance and that affects the first part of Equation (2).

In addition, the probability of collapse in 50 years of the four frames is calculated at the midfault and end-of-fault sites, for site-to-source distances equal to 5, 10 and 15 km. To do so, a Poisson distribution of the earthquake occurrences is utilized, which is given by the following equation:

$$P[\text{Collapse in 50 years}] = 1 - e^{-vt} \tag{8}$$

where t is the time in years and v is the mean annual frequency of collapse, computed by integrating the collapse probability distribution, i.e. the fragility curve of each frame, with the rate of exceedance for each spectral acceleration and site of interest. The results of this calculation are presented in Table 2.

(a) (b)

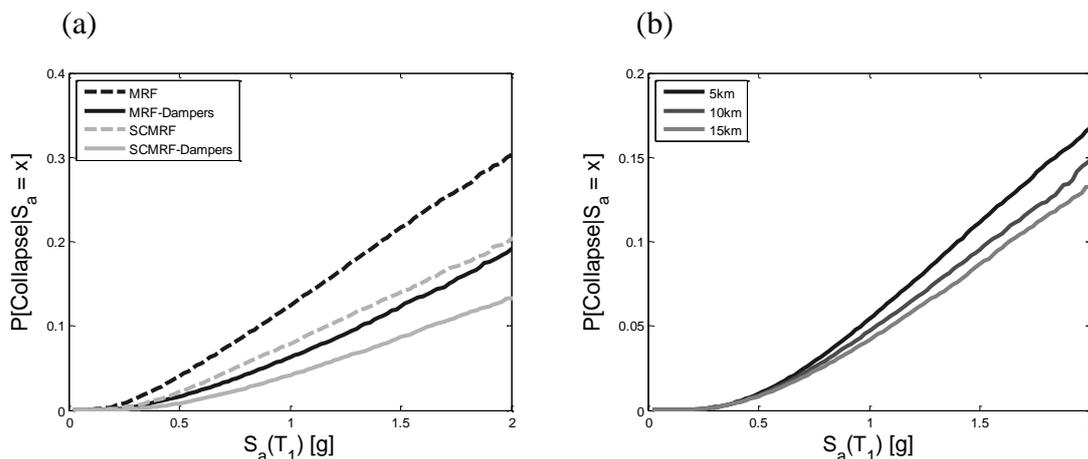**Fig. 10** Collapse fragility functions for **a)** all the frames when located at midfault sites for a site-to-source distance equal to 15 km; and **b)** the SC-MRF with viscous dampers at three different midfault sites.

A trend showing reduction of collapse risk as the distance from the fault increases is evident from the results in Table 2. When the site-to-source distance is decreased from 15 to

10 km, the probability of the frames collapsing in 50 years is increased by a factor varying from 1.8 to 1.9 at both the midfault and end-of-fault sites. In addition, the collapse risk of the frames located 5 km away from the fault is 4.0 to 5.0 and 4.7 to 5.0 higher than that associated with a distance of 15 km from the fault, for the midfault and end-of-fault sites, respectively. The aforementioned observations suggest a large increase in the collapse risk of the structures due to near-fault directivity.

When comparing the collapse risk at each of midfault and end-of-fault sites for a particular frame, it is observed that the collapse risk is not as largely affected by the relative position of the site to the fault axis as it is by the distance to the fault. However, slightly larger values of the probability of collapse of the frames are found at the end-of-fault sites.

Table 2 Probability of collapse in 50 years

| | P[Collapse in 50 yrs] | | | | | |
| | Midfault sites | | | End-of-fault sites | | |
Frame	5km	10km	15km	5km	10km	15km
MRF	7.4%	3.3%	1.8%	7.6%	3.4%	1.9%
MRF-Dampers	3.5%	1.4%	0.7%	3.6%	1.5%	0.8%
SC-MRF	5.0%	2.1%	1.2%	5.2%	2.3%	1.3%
SC-MRF-Dampers	2.4%	0.9%	0.5%	2.5%	1.0%	0.5%

The results in Table 2 show that the SC-MRF has approximately 32%, 35% and 37% reduced collapse risk compared to the MRF for site-to-source distances equal to 5, 10 and 15 km, respectively, at both the midfault and end-of-fault sites. These results demonstrate that post-tensioning is very effective in reducing the collapse risk. Moreover, the MRF with viscous dampers has 53%, 58% and 60% lower probability of collapse in 50 years than that of the MRF for site-to-source distances equal to 5, 10 and 15 km, respectively, at the midfault sites. A similar trend was observed at the end-of-fault sites. These results demonstrate that supplemental viscous damping is very effective in reducing the collapse risk. Finally, the SC-MRF with viscous dampers has the best performance with probabilities of collapse in 50 years significantly lower than those of the MRF. In this case the decrease in the collapse risk ranges from 67% to 74%.

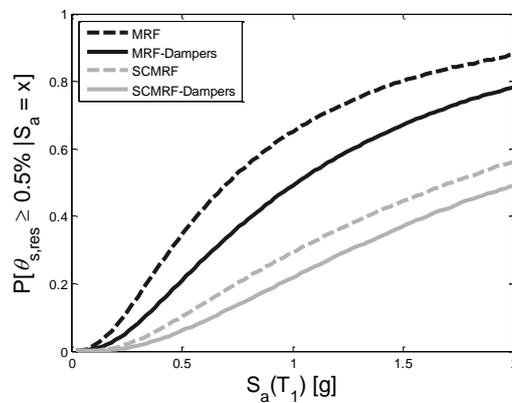## 10 Residual drift performance of the frames in the near-source

Fig. 11 Residual drift fragility functions for all the frames located at midfault sites for site-to-source distance equal to 15 km.

McCormick et al. (2008) suggested a limit value of 0.5% for the permissible residual story drift, $\theta_{s,res}$, beyond which is not financially viable to repair a steel building. Using the methodology described in Section 8, fragility curves that provide the probability of exceedance of $\theta_{s,res}$ equal to 0.5% were constructed and shown in Fig. 11, for the 15 km distant midfault sites. The fragility curves indicate that the frames equipped with post-tensioned connections have the best residual drift performance. The SC-MRF with viscous dampers exhibits the lower probabilities of exceedance of $\theta_{s,res}$ equal to 0.5%.

The probability of exceedance of the 0.5% $\theta_{s,res}$ limit in 50 years is computed at the midfault and end-of-fault sites, for site-to-source distances equal to 5, 10 and 15 km, by utilizing Equation (8). The results are listed in Table 3. Increased residual drift risk at sites closer to the fault is observed from the results of Table 3. The probability of exceeding the specified limit of $\theta_{s,res}$ in 50 years of the frames located at 10 km distance sites, is 1.4 to 1.7 larger than that when they are located 15 km away from the fault, at both the midfault and end-of-fault sites. When the site-to-source distance is decreased from 15 to 5 km the probability of the frames exceeding the specified limit of $\theta_{s,res}$ is increased by a factor varying from 2.2 to 3.5 for both the midfault and end-of-fault sites. In addition, the residual drift performance of the frames is not as largely affected by the relative position of the site to the fault axis as it is by the distance to the fault. However, slightly larger values of the probability of exceeding $\theta_{s,res}$ equal to 0.5% are found at the end-of-fault sites.

The results in Table 3 show that the SC-MRF has approximately 55%, 64% and 68% less probability of exceedance of $\theta_{s,res}$ equal to 0.5% in 50 years than that of the MRF for site-to-source distances equal to 5, 10 and 15 km, respectively, at the midfault sites. A similar trend is observed at the end-of-fault sites. These results demonstrate that post-tensioning significantly improves the residual drift performance of the MRF. The MRF with viscous dampers has 32%, 39% and 43% reduced probability of exceeding $\theta_{s,res}$ equal to 0.5% in 50 years than that of the MRF for site-to-source distances equal to 5, 10 and 15 km, respectively, at both the midfault and end-of-fault sites. These results highlight that supplemental damping is very efficient in reducing $\theta_{s,res}$. Moreover, the SC-MRF with viscous dampers has the best residual drift performance with probabilities of exceedance of $\theta_{s,res}$ equal to 0.5% in 50 years significantly lower than those of the MRF. In this case the decrease in these probabilities ranges between 70% and 81%, at both the midfault and end-of-fault sites.

Table 3 Probability of exceedance of $\theta_{s,res}$ equal to 0.5% in 50 years

| | $P[\theta_{s,res} \geq 0.5\%$ in 50 yrs] | | | | | |
| | Midfault sites | | | End-of-fault sites | | |
Frame	5km	10km	15km	5km	10km	15km
MRF	36.8%	23.9%	16.8%	37.5%	24.7%	17.6%
MRF-Dampers	25.0%	14.6%	9.6%	25.7%	15.2%	10.1%
SC-MRF	16.5%	8.7%	5.4%	17.0%	9.1%	5.7%
SC-MRF-Dampers	11.0%	5.4%	3.2%	11.4%	5.7%	3.4%

Table 4 Probability of exceedance of $\theta_{s,res}$ equal to 1.0% in 50 years

| | $P[\theta_{s,res} \geq 1.0\%$ in 50 yrs] | | | | | |
| | Midfault sites | | | End-of-fault sites | | |
Frame	5km	10km	15km	5km	10km	15km
MRF	24.3%	14.1%	9.2%	25.0%	14.7%	9.8%
MRF-Dampers	15.8%	8.3%	5.1%	16.3%	8.7%	5.4%
SC-MRF	11.1%	5.4%	3.2%	11.5%	5.7%	3.4%
SC-MRF-Dampers	6.9%	3.1%	1.7%	7.1%	3.3%	1.9%

Table 5 Probability of exceedance of $\theta_{s,res}$ equal to 1.5% in 50 years

| | P[$\theta_{s,res}$ ≥ 1.5% in 50 yrs] | | | | | |
| | Midfault sites | | | End-of-fault sites | | |
Frame	5km	10km	15km	5km	10km	15km
MRF	18.4%	9.9%	6.2%	19.0%	10.4%	6.6%
MRF-Dampers	10.9%	5.3%	3.1%	11.3%	5.6%	3.3%
SC-MRF	9.1%	4.3%	2.5%	9.5%	4.5%	2.6%
SC-MRF-Dampers	5.4%	2.4%	1.3%	5.7%	2.5%	1.4%

To evaluate the influence of different values of $\theta_{s,res}$ used as limits for the above probabilities, two additional threshold values of $\theta_{s,res}$ were considered, i.e.: 1% and 1.5%. The results are presented in Tables 4 and 5. The SC-MRF has approximately 54%, 62% and 66% less probability of exceedance of $\theta_{s,res}$ equal to 1% in 50 years than that of the MRF for site-to-source distances equal to 5, 10 and 15 km, respectively, at both the midfault and end-of-fault sites. The MRF with viscous dampers has approximately 35%, 41% and 45% reduced probability of exceeding $\theta_{s,res}$ equal to 1% in 50 years than that of the MRF for site-to-source distances equal to 5, 10 and 15 km, respectively, at both the midfault and end-of-fault sites. Table 4 also shows that the SC-MRF with viscous dampers exhibits the best performance with probabilities of exceedance of $\theta_{s,res}$ equal to 1% in 50 years significantly lower than those of the MRF.

Similar conclusions can be drawn based on the results shown in Table 5. In this case the reduction in the probability of exceedance of $\theta_{s,res}$ equal to 1.5% in 50 years provided by the SC-MRF, the MRF with viscous dampers and the SC-MRF with viscous dampers ranges between 50% and 60%, 40% and 50% and 70% and 79%, respectively, at both the midfault and end-of-fault sites.

11. Conclusions

The potential of SC-MRFs and viscous dampers to reduce the collapse risk and improve the residual drift performance of steel buildings in near-fault regions has been evaluated. The evaluation was based on a prototype steel building designed to use different seismic-resistant frames, i.e.: MRFs; MRFs with viscous dampers; SC-MRFs; and SC-MRFs with viscous dampers. The frames were modeled in OpenSees where material and geometrical nonlinearities are taken into account as well as stiffness and strength deterioration. A database of 91 near-fault, pulse-like ground motions with varying pulse periods was used to conduct IDA. The probability of collapse and the probability of exceeding different residual story drift threshold values were then calculated as a function of the ground motion intensity and the period of the velocity pulse. Finally, the results of IDA were combined with NS-PSHA to assess and compare the collapse risk and the residual drift performance of the different seismic-resistant frames.

On the basis of the results presented in this paper, the following conclusions can be drawn:

1. The collapse risk of the frames significantly increases as the distance from the fault decreases. In particular, the collapse risk of the frames located 5 km away from the fault is 4.0-5.0 and 4.7-5.0 higher than that at a distance of 15 km from the fault, for midfault and end-of-fault sites, respectively.

2. When comparing the collapse risk of a specific frame at midfault and end-of-fault sites, it is observed that the collapse risk is not as largely affected by the relative position of the site to the fault axis as it is by the distance to the fault.

3. Post-tensioning significantly improves the collapse resistance, i.e. the SC-MRF achieves 32%, 35% and 37% reductions in collapse risk compared to that of the MRF for site-to-source distances equal to 5, 10 and 15 km, respectively.

4. Supplemental viscous damping is very effective in reducing the collapse risk, i.e. the MRF with viscous dampers has 53%, 58% and 60% lower probability of collapse in 50 years than that of the MRF for site-to-source distances equal to 5, 10 and 15 km, respectively.

5. Residual drifts performance is significantly affected by forward directivity. In particular, when the site-to-source distance is decreased from 15 to 5 km the probability of exceeding a $\theta_{s,res}$ limit value of 0.5% increases by a factor of 2.2-3.5.

6. Post-tensioning significantly improves the residual drift performance of the frames. The SC-MRF achieves probabilities of exceedance of limit values of the $\theta_{s,res}$ equal to 0.5%, 1.0% and 1.5% in 50 years equal to 30%-45% of those of the MRF.

7. Viscous damping is very effective in reducing the residual drifts in the near-source. In particular, the MRF with viscous dampers achieves probabilities of exceedance of limit values of the $\theta_{s,res}$ equal to 0.5%, 1.0% and 1.5% in 50 years equal to 50%-60% of those of the MRF.

8. Combining the post-tensioning and supplemental viscous damping technologies is a very effective way of achieving superior collapse resistance and residual drifts performance in the near-source. In particular, the SC-MRF with viscous dampers has probabilities of collapse in 50 years equal to 25%-35% of the MRF. Moreover, the SC-MRF with viscous dampers achieves probabilities of exceedance of limit values of the $\theta_{s,res}$ equal to 0.5%, 1.0% and 1.5% in 50 years equal to 20%-30% of those of the MRF.

Acknowledgements

References

Alavi B, Krawinkler H (2004) Behavior of moment-resisting frame structures subjected to near-fault ground motions. Earthquake Engineering and Structural Dynamics 33:687–706.

Baker JW, Cornell CA (2006) Spectral shape, epsilon and record selection. Earthquake Engineering and Structural Dynamics 35(9):1077–1095.

Baker JW (2007) Quantitative Classification of Near-Fault Ground Motions Using Wavelet Analysis. Bulletin of the Seismological Society of America 97(5):1486–1501.

Bertero VV, Mahin SA, Herrera RA (1978) Aseismic design implications of near-fault San Fernando earthquake records. Earthquake Engineering and Structural Dynamics 6(1):31–42.

Champion C, Liel A (2012) The effect of near-fault directivity on building seismic collapse risk. Earthquake Engineering and Structural Dynamics 41(10):1391–1409.

Chioccarelli E, Iervolino I (2010) Near-Source Seismic Demand and Pulse-Like Records: a Discussion for L'Aquila Earthquake. Earthquake Engineering and Structural Dynamics 39(9):1039–1062.

Chioccarelli E, Iervolino I (2013) Near-source seismic hazard and design scenarios. Earthquake Engineering and Structural Dynamics 42(4):603-622.

Chioccarelli E, Iervolino I (2014) Sensitivity analysis of directivity effects on PSHA. Bollettino di Geofisica Teorica e Applicata 55(1):41-53.

Chopra AK, and Chintanapakdee C (2003) Comparing response of SDF systems to near-fault and far-fault earthquake motions in the context of spectral regions. Earthquake Engineering and Structural Dynamics 30:1769–1789.

Chou CC, Lai YJ (2009) Post-tensioned self-centering moment connections with beam bottom flange energy dissipators. Journal of Constructional Steel Research 65(10-11):1931-1941.

Chou C-C, Tsai K-C, Yang W-C (2009) Self-centering steel connections with steel bars and a discontinuous composite slab. Earthquake Engineering and Structural Dynamics 38(4):403-422.

Christopoulos C, Filiatrault A, Uang C-M (2002) Post-tensioned energy dissipating connections for moment resisting steel frames. Journal of Structural Engineering ASCE 128(9):1111–1120.

Dimopoulos A, Karavasilis TL, Vasdravellis G, Uy B (2013) Seismic design, modelling and assessment of self-centering steel frames using post-tensioned connections with web hourglass shape pins. Bulletin of Earthquake Engineering 11(5):1797-1816.

EC8 (2013) Eurocode 8. Design of structures for earthquake resistance.

FEMA P695 (2008) Quantification of building seismic performance factors. ATC-63 Project. Applied Technology Council. CA, USA.

Garlock M, Sause R, Ricles JM (2007) Behavior and design of posttensioned steel frame systems. Journal of Structural Engineering 133(3):389-399.

Hamidia M, Filiatrault A, Aref A (2014) Simplified seismic sidesway collapse analysis of frame buildings. Earthquake Engineering and Structural Dynamics 43(3):429–448.

Haselton CB, Baker JW, Liel AB, Deierlein GG (2011) Accounting for Ground Motion Spectral Shape Characteristics in Structural Collapse Assessment Through an Adjustment for Epsilon. Journal of Structural Engineering 137(3):332–344.

Iervolino I, Cornell CA (2008) Probability of Occurrence of Velocity Pulses in Near-Source Ground Motions. Bulletin of the Seismological Society of America 98(5):2262–2277.

Kam WY, Pampanin S, Palermo A, Car AJ (2010) Self-centering structural systems with combination of hysteretic and viscous energy dissipations. Earthquake Engineering and Structural Dynamics 39(10): 1083-1108.

Karavasilis TL, Makris N, Bazeos N, Beskos, DE (2010) Dimensional response analysis of multistory regular steel MRF subjected to pulselike earthquake ground motions. Journal of Structural Engineering; 136(8):921–932.

Karavasilis TL, Ricles JM, Sause R, Chen C (2011) Experimental evaluation of the seismic performance of steel MRFs with compressed elastomer dampers using large-scale real-time hybrid simulation. Engineering Structures 33(6):1859-1869.

Karavasilis TL, Sause R, Ricles JM (2012) Seismic design and evaluation of steel MRFs with compressed elastomer dampers. Earthquake Engineering and Structural Dynamics 41(3):411-429.

Karavasilis TL, Seo C-Y. (2011) Seismic structural and non-structural performance evaluation of highly damped self-centering and conventional systems. Engineering Structures 33: 2248-2258.

Kim HJ, Christopoulos C (2008a) Friction damped posttensioned self-centering steel moment-resisting frames. Journal of Structural Engineering 134(11):1768-1779.

Kim HJ, Christopoulos C (2008b) Seismic design procedure and seismic response of post-tensioned self-centering steel frames. Earthquake Engineering and Structural Dynamics 38(3): 355-376.

Krawinkler H (1978) Shear Design of Steel Frame Joints. Engineering Journal, AISC 15(2): 82-91.

Kurama YC (2000) Seismic design of unbonded post-tensioned precast concrete walls with supplementary viscous damping. ACI Structural Journal 97(3):648–658.

Liel AB, Haselton CB, Deierlein GG, Baker JW (2009) Incorporating Modeling Uncertainties in the Assessment of Seismic Collapse Risk of Buildings. Structural Safety 31(2):197–211.

Lignos DG, Krawinkler H (2011) Deterioration Modeling of Steel Components in Support of Collapse Prediction of Steel Moment Frames under Earthquake Loading. Journal of Structural Engineering 137(11):1291-1302.

Luco N, Ellingwood BR, Hamburger RO, Hooper JD, Kimball JK, Kircher CA (2007) Risk-Targeted versus Current Seismic Design Maps for the Conterminous United States. SEAOC 2007 Convention Proceedings.

Makris N, Psychogios T (2006) Dimensional response analysis of yielding structures with first-mode dominated response. Earthquake Engineering and Structural Dynamics 35(10):1202–1224.

Mavroeidis GP, Dong G, Papageorgiou AS (2004) Near-fault ground motions and the response of elastic and inelastic,single-degree-of-freedom (SDOF) systems. Earthquake Engineering and Structural Dynamics 33:1023–1049.

Mazzoni S, McKenna F, Scott M, Fenves G (2006) Open system for earthquake engineering simulation (OpenSees). User Command Language Manual, Pacific Earthquake Engineering Research Center, University of California, Berkeley.

McCormick J, Aburano H, Ikenaga M, Nakashima M (2008) Permissible residual deformation levels for building structures considering both safety and human elements. The 14th World Conference on Earthquake Engineering, Beijing, China, October 12-17.

Newell J, Uang C-M (2006) Cyclic behaviour of steel columns with combined high axial load and drift demand. Report No. SSRP-06/22. Department of Structural Engineering, University of California, San Diego, La Jolla.

PEER (2015) Pacific Earthquake Engineering Research Center. NGA Database. http://peer.berkeley.edu/nga/.

Ricles JM, Sause R, Garlock MM, Zhao C (2001) Postensioned seismic-resistant connections for steel frames. Journal of Structural Engineering ASCE 127(2):113–121.

Rojas P, Ricles JM, Sause R (2004) Seismic performance of post-tensioned steel moment resisting frames with friction devices. Journal of Structural Engineering 131(4):529-540.

Ruiz-Garcia J, Miranda E (2006) Residual displacement ratios for assessment of existing structures. Earthquake Engineering and Structural Dynamics 35:315-336.

Scott MH, Fenves GL (2006) Plastic hinge integration methods for force –based neam-column elements. Journal of Structural Engineering 132(2):244-252.

Seo C-Y, Karavasilis TL, Ricles JM, Sause R (2014) Seismic performance and probabilistic collapse resistance assessment of steel moment resisting frames with fluid viscous dampers. Earthquake Engineering and Structural Dynamics 43(14):2135-2144.

Shahi SK, Baker JW (2011) An Empirically Calibrated Framework for Including the Effects of Near Fault Directivity in Probabilistic Seismic Hazard Analysis. Bulletin of the Seismological Society of America 101(2):742–755.

Somerville PG, Smith NF, Graves RW, Abrahamson NA (1997) Modification of Empirical Strong Ground Motion Attenuation Relations to Include the Amplitude and Duration Effects of Rupture Directivity. Seismological Research Letters 68(1):199–222.

Somerville PG. Magnitude Scaling of the Near Fault Rupture Directivity Pulse (2003) Physics of the Earth and Planetary Interiors 137(1):201–212.

Tothong P, Cornell CA, Baker JW (2007) Explicit Directivity-Pulse Inclusion in Probabilistic Seismic Hazard Analysis. Earthquake Spectra 23(4):867–891.

Tsai KC, Chou CC, Lin CL, Chen PC, Jhang SJ (2008) Seismic self-centering steel beam-to-column moment connections using bolted friction devices. Earthquake Engineering and Structural Dynamics 37(4):627-645.

Tzimas AS, Dimopoulos AI, Karavasilis TL (2015) EC8-based seismic design and assessment of self-centering steel frames with viscous dampers. Journal of Constructional Steel Research 105:60-73.

Vamvatsikos D, Cornell CA (2002) Incremental dynamic analysis. Earthquake Engineering Structural Dynamics 31(3):491-514.

Vasdravellis G, Karavasilis TL, Uy B (2013a) Finite element models and cyclic behaviour of self-centering post-tensioned connections with web hourglass pins. Engineering Structures 52:1-16.

Vasdravellis G, Karavasilis TL, Uy B (2013b) Large-scale experimental validation of steel post-tensioned connections with web hourglass pins. Journal of Structural Engineering ASCE 139(6):1033-1042.

Veletsos A, and Newmark NM (1960) Effect of inelastic behaviour on response of simple systems to earthquake motions. Proc., 2nd World Conf. on Earthquake Engineering Vol. II, Tokyo, 895–912.

Wells DL, Coppersmith KJ (1994) New empirical relationships among magnitude, rupture length, rupture width, rupture area, and surface displacement. Bulletin of the Seismological Society of America 84(4):974-1002.

Wolski M, Ricles JM, Sause R (2009) Experimental study of a self-centering beam-column connection with bottom flange friction device. Journal of Structural Engineering 135(5):479-488.